Physics and Chemistry of Minerals (2024) 51:12
https://doi.org/10.1007/s00269-024-01274-9

ORIGINAL PAPER

Thermal evolution of metamict davidite-(La) from the Radium Hill, Australia: recrystallization and thermal expansion

Ruiqi Chen[1,2] · Oleg I. Siidra[1,3] · Valery L. Ugolkov[3] · Vera A. Firsova[3] · Natalia S. Vlasenko[4] · Angel M. Arevalo-Lopez[2] · Marie Colmont[2] · Vladimir N. Bocharov[4]

Received: 21 October 2023 / Accepted: 4 March 2024

Abstract

Aside from its economic value, davidite and its synthetic analogs may have potential applications in materials science. The unique properties of the crichtonite group minerals, including davidite-(La), make them attractive candidates for high-level waste (HLW) immobilization. We studied the thermal evolution of the metamict davidite-(La) from the Radium Hill, Australia. The investigation of the temperature-induced crystallization process was conducted, and the thermal expansion coefficients (TEC) for the recrystallized davidite (RD) were determined for the first time. Our results demonstrate that RD has relatively low TEC indicating its thermophysical stability. The following TECs of davidite- (La) for the temperature range 25–1200 °C were obtained: $\overline{\alpha}_a = \overline{\alpha}_b = 9.96\ (3) \times 10^{-6}\ ^{\circ}C^{-1}$; $\overline{\alpha}_c = 10.79\ (4) \times 10^{-6}\ ^{\circ}C^{-1}$. The character of the thermal expansion is in agreement with the structure characterized by layers stacked along the *c* axis. The volume TEC $\alpha_V = 24.81\ (47)$—$36.80\ (48) \times 10^{-6}\ ^{\circ}C^{-1}$. Davidite-(La) exhibits an almost isotropic thermal expansion and shows one of the most superior thermal performances in comparison to the other mineral-like phases utilized for the immobilization of HLW.

Keywords Metamict minerals · Davidite- (La) · Crichtonite group minerals · Thermal expansion

Introduction

Davidite-(La) is a rare earth mineral and a member of the crichtonite group. It crystallizes in a trigonal symmetry, space group $R\,\overline{3}$ (Rastsvetaeva 2020). There are six cation sites in crystal structures of crichtonite group minerals (e.g. Gatehouse et al. 1979; Chukanov et al. 2020). In davidite-(La), *M*0 site can be occupied by La, Ce and Ca, *M*1 = U, Y, La, *M*2 = Fe^{2+}, *M*3 = Fe^{3+}, Ti, Cr, and *M*4, *M*5 sites are predominantly occupied by Ti (Rastsvetaeva 2020) (Fig. 1). These coordination polyhedra condense into layers stacked in a …*ABCBCACAB*… sequence. Davidite, a mineral known for its high uranium content, was mined for uranium in the Radium Hill area in Australia (Ludwig and Cooper 1984). It is estimated that ~ 970 tons of davidite ore were mined between 1906 and 1944, producing 852 tons of U_3O_8 (Lottermoser and Ashley 2005).

✉ Oleg I. Siidra
o.siidra@spbu.ru

Ruiqi Chen
st051720@student.spbu.ru

Valery L. Ugolkov
ugolkov.52@gmail.com

Vera A. Firsova
va_firsova@mail.ru

Natalia S. Vlasenko
n.vlasenko@spbu.ru

Angel M. Arevalo-Lopez
angel.arevalo-lopez@univ-lille.fr

Marie Colmont
marie.colmont@centralelille.fr

Vladimir N. Bocharov
regbvn@gmail.com

[1] Department of Crystallography, Institute of Earth Sciences, St. Petersburg State University, University Emb. 7/9, 199034 St. Petersburg, Russia

[2] Unité de Catalyse et Chimie du Solide, University Lille, CNRS, Centrale Lille, University Artois, UMR 8181, UCCS, 59000 Lille, France

[3] Institute of Silicate Chemistry, Russian Academy of Sciences, 2 Makarova Emb., St Petersburg 199034, Russia

[4] Geomodel Resource Center, St. Petersburg State University, 199034 St. Petersburg, Russia

Published online: 22 April 2024

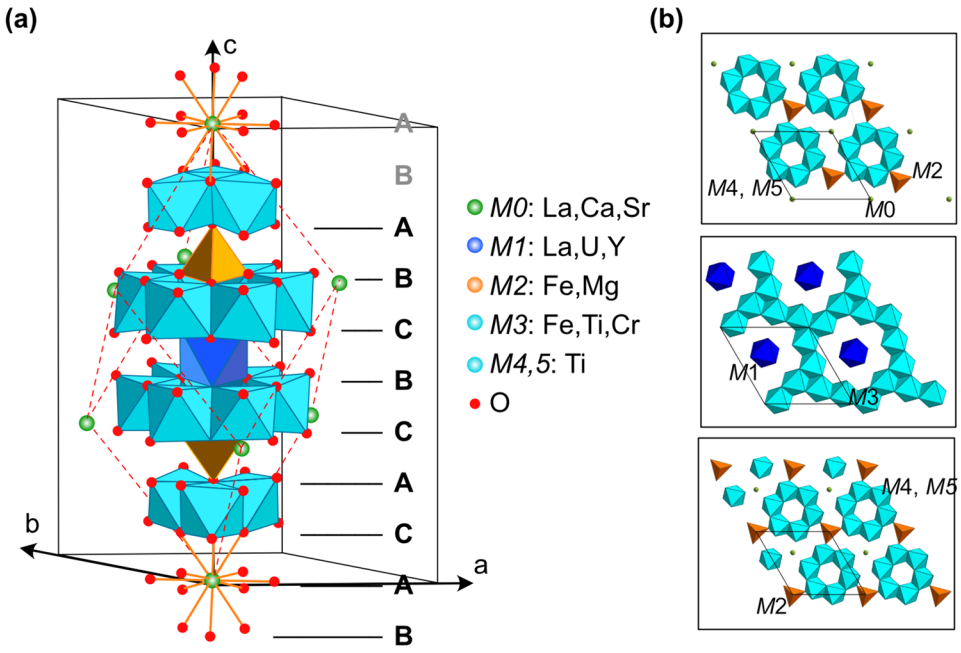

Fig. 1 The crystal structure of davidite-(La) (**a**). It is characterized by a nine-layer stacking sequence …*ABCBCACAB*… (drawn after Gatehouse et al. 1979). The general projection of layers along the *c* axis (**b**)

Aside from its economic value, davidite and its synthetic analogs may have potential applications in materials science. The crichtonite group minerals, including davidite-(La), possess unique properties that make them attractive candidates for nuclear waste immobilization (Lumpkin 2006; Yudintsev et al. 2001; Zhang et al. 2013). They have been found to exhibit extraordinarily high chemical capacity and resistance to radiation, which validate the powerful waste loading of crichtonite structure (Gong et al. 1994). As a host phase for radioactive wastes, crichtonite may form in multi-phase ceramics (Yudintsev et al. 2022). The thermal behavior of different phases in these ceramics can cause strains and cracks, which reduces the material's effectiveness. Hence, it is essential to investigate the thermal properties of different phases, including crichtonite, to avoid a severe mismatch between phases.

In this paper, we present a study examining the temperature-induced crystallization of the metamict davidite-(La). The thermal expansion of the crystalline davidite was studied for the first time. This could potentially furnish us with valuable insights into the behavior of radioactive elements in natural systems, thereby facilitating the management and disposal of radioactive waste.

Experimental

Sample origin

Figure 2 shows the host rock and selected grains of the metamict davidite-(La). Specimen originates from the Radium Hill mine, Australia (Whittle 1954, 1959). It was stored in the previously existed collection of the radioactive minerals at the department of the Mineral Deposits, Saint-Petersburg State University, Russia. Due to several isotope distribution events, it is difficult to determine the age of davidite-(La) from Radium Hill, but primary mineralization in Radium Hill is estimated to date back to 1580 million years ago (Ludwig and Cooper 1984).

The initial metamict davidite grains, labeled Dav.1-Dav.5, were hand-picked from the host rock. Dav.4 and Dav.5 grains were each placed into a Pt crucible and kept at 1200 °C for 24 h in air in a Nabertherm furnace followed by cooling to 25 °C with a cooling rate of 5 °C/min.

In the text below, we refer to metamict davidite-(La) as **MD** and recrystallized davidite-(La) obtained by heating a metamict sample as **RD**.

Fig. 2 Metamict davidite-(La) (**MD**) in the host rock and grains selected for the study

Chemical composition

The **MD** and **RD** grains were prepared by mounting them in an epoxy resin. The samples were studied using the scanning electron microscope Hitachi S-3400N, equipped with a spectrometer Oxford Instruments X-Max 20. Photos of the samples were taken in the backscattered electron mode (BSE). Quantitative analyses were performed with an accelerating voltage of 20 kV and a beam current of 1.8 nA. Acquisition time was 30 s, with a resolution up to 4 nm. The following standards were used for the quantification: MAC (Micro Analysis Consultants Ltd., United Kingdom) and Geller reference standards (Geller microanalytical laboratory).

Raman spectroscopy

Raman spectra were acquired on a Horiba Jobin–Yvon LabRam HR800 Raman spectrometer, equipped with Olympus BX41 optical microscope with a resolution of 2 cm^{-1} and the laser beam spot size of 5 µm. Raman spectra were excited by an Ar^{+} laser (514 nm). Baseline correction was used to improve the signal-to-noise ratio using CrystalSleuth software.

High-temperature powder X-ray diffraction (HTXRD)

The recrystallization process of the **MD** was studied under heating in air by HTXRD using a Rigaku Ultima IV diffractometer (CoKα radiation, 40 kV/30 mA, Bragg–Brentano geometry, PSD D-Tex Ultra) with a thermo-attachment in the range 20–600 °C with the temperature steps of 100 °C and in the range 600–1200 °C with the temperature steps of 25 °C. Phase analysis was performed based on PDF-2 database (2020), PDXL (Rigaku 2016) and TOPAS V.5.0 (Bruker 2011) software.

The **RD** sample was studied using the same equipment in a range of 25–1200 °C with the temperature steps of 25 °C. The fine-powdered samples were deposited on a platinum sample holder ($20 \times 12 \times 1.5$ mm^3) from an ethanol suspension. An external Si standard was used before the measurements to control the 2θ correctness. The calculations of the unit-cell parameters were performed using the program package Topas 5.0, whereas the visualization and calculation of the thermal-expansion parameters tensor were performed using the Rietveld-To-Tensor program package (Bubnova et al. 2018).

Thermal analysis

MD was studied using a NETZSCH STA 429 thermal analyzer in the range 40–1300 °C (20 °C/min). The powdered sample was placed in a corundum crucible.

Results

Chemical composition

The results of electron microprobe analysis are presented in Table 1. Based on 38 O atoms per formula unit, the following mineral formula was calculated (17 points) for the **MD** sample: $(La_{0.48},Ce_{0.36},Ca_{0.09})_{\Sigma=0.93}$ $(U_{0.29},Th_{0.01}, Pb_{0.02}, Y_{0.37},Nb_{0.03},Nd_{0.01},Sm_{0.01},Gd_{0.01},Dy_{0.05},Er_{0.04},Yb_{0.07})_{\Sigma=0.91}$ $(Mn^{2+}_{0.05},Fe^{2+}_{1.97})_{\Sigma=2.02}$ $(V_{0.20},Cr_{0.24}, Fe^{3+}_{5.32})_{\Sigma=5.75}$ $Ti_{12.14}$ $(O_{36.69},H_2O_{1.31})_{\Sigma=38}$.

The backscattered electron (BSE) image in Fig. 3 reveals that **MD** grains exhibit zoning. The brighter zones in BSE correspond to higher U and Th contents but lower Y and rare earth elements (REE). The darker zones in BSE exhibit the lower U and Th but higher Y and REE contents. This zonal distribution of chemical elements may indicate changes in the crystallization conditions. However, this pattern may also be linked to the subsequent post-crystallization processes. Previous studies have indicated that rocks containing davidite-(La) at Radium Hill underwent at least two stages of isotope redistribution, resulting in losses of uranium and thorium (Ludwig and Cooper 1984).

Heat-treated grains Dav. 4, 5 (i.e. **RD**) have the formula: $(La_{0.50},Ce_{0.37},Ca_{0.11})_{\Sigma=0.98}$ $(U_{0.45}, Th_{0.01},Pb_{0.02},Y_{0.34},Nb_{0.01},Nd_{0.02},Sm_{0.02},Gd_{0.00},Dy_{0.04},Er_{0.05},Yb_{0.09})_{\Sigma=1.05}Mn^{2+}_{0.06}$ $(V_{0.18},Cr_{0.23},Fe^{3+}_{6.14})_{\Sigma=6.56}Ti_{12.35}O_{38}$. BSE image of two heat-treated grains is shown in Fig. 4, where the mineral grains exhibit a porous texture. There is an irregular-shaped inclusion with a diameter of about 10 µm in Dav. 5, which has a chemical composition of uraninite UO_2. Bright spots with a diameter smaller than 1 µm can be observed (Fig. 4). However, due to their extremely small size, the chemical composition of these spots cannot be determined unambiguously. These small grains have a higher U and Y content comparing to the grayish "background", but a lower Fe and Ca content. As it can be seen from the BSE images acquired before and after the heating (Fig. 3, 4), there is a redistribution of elements. Other phases have crystallized in addition to davidite-(La) (see below).

Raman spectroscopy

Raman spectra of the **MD** and **RD** samples are represented in Fig. 5. Obtained spectra for both samples show typical bands observed for the crichtonite-group minerals in the regions of 100–200 cm^{-1}, 300–450 cm^{-1}, and 700–800 cm^{-1} (Alifirova et al. 2020). We have compared the collected spectra with those of davidite-(La) (Frost and Reddy 2011), and other mineral species of the crichtonite group (Alifirova et al. 2020) studied earlier. Despite the fact that one of the samples studied earlier by Frost and Reddy (2011) is also

Table 1 Chemical composition (wt.%) of the metamict (**MD**) (grains Dav.1, Dav.2, Dav.3 grains) and recrystallized (**RD**) (grains Dav. 4 and Dav. 5) davidite-(La). The water content is obtained by TGA

	Initial metamict sample			Heat-treated			*a.p.f.u*	Initial	Heat-treated
	Average	Range	e.s.d	Average	Range	e.s.d	O^{2-}	38	38
CaO	0.28	0.22–0.37	0.04	0.35	0.26–0.69	0.15	La^{3+}	0.48	0.50
TiO_2	51.66	50.73–52.55	0.43	51.47	47.29–53.32	2.10	Ce^{3+}	0.36	0.37
V_2O_5	0.95	0.77–1.16	0.12	0.87	0.62–1.07	0.15	Ca^{2+}	0.09	0.11
Cr_2O_3	0.95	0.68–1.19	0.14	0.92	0.8–1.08	0.08	(La,Ce,Ca)	0.93	0.99
MnO	0.18	0–0.37	0.11	0.22	0.12–0.3	0.06	U^{4+}	0.29	0.45
Total Fe	30.19	29.78–30.62	0.25	25.57	24.11–28.37	1.54	Th^{4+}	0.01	0.01
Fe_2O_3	22.65			25.57			Pb^{2+}	0.02	0.02
FeO	7.55			n.a.			Y^{3+}	0.37	0.34
Y_2O_3	2.24	1.85–2.45	0.13	1.98	1.41–3.59	0.78	Nb^{5+}	0.03	0.01
Nb_2O_5	0.23	0–0.39	0.09	0.09	0–0.51	0.19	Nd^{3+}	0.01	0.02
La_2O_3	4.15	3.97–4.56	0.15	4.26	3.6–4.91	0.48	Sm^{3+}	0.01	0.02
Ce_2O_3	3.11	2.85–3.34	0.13	3.15	2.85–3.47	0.25	Gd^{3+}	0.01	0.00
Nd_2O_3	0.06	0–0.49	0.13	0.14	0–0.56	0.22	Dy^{3+}	0.05	0.04
Sm_2O_3	0.03	0–0.28	0.09	0.06	0–0.36	0.13	Er^{3+}	0.04	0.05
Gd_2O_3	0.10	0–0.31	0.14	0.04	0–0.26	0.10	Yb^{3+}	0.07	0.09
Dy_2O_3	0.54	0–0.84	0.24	0.42	0–0.73	0.31	(U,Y,REE)	0.91	1.05
Er_2O_3	0.42	0–0.66	0.20	0.55	0–1.11	0.42	Mn^{2+}	0.05	0.06
Yb_2O_3	0.78	0.44–1.13	0.18	0.97	0.61–1.57	0.31	Fe^{2+}	1.97	n.a.
PbO	0.18	0–0.4	0.14	0.23	0–0.37	0.12	(Mn^{2+},Fe^{2+})	2.02	0.06
ThO_2	0.15	0–0.38	0.13	0.08	0–0.26	0.12	$V^{5}+$	0.20	0.18
UO_2	4.15	3.64–5.04	0.41	6.34	3.8–8.68	1.48	Cr^{3+}	0.24	0.23
Total	100.36	98.69–101.71	0.88	97.69	97.09–98.41	0.52	Fe^{3+}	5.32	6.14
H_2O*	1.26			n.a.			(Fe^{3+},Cr^{3+})	5.75	6.56
							Ti^{4+}	12.14	12.35
							H_2O	1.31	n.a.

from the Radium Hill, its Raman spectrum slightly differs. The peak at 641 cm^{-1} has an increased intensity, while the bands at 732 and 809 cm^{-1} have lower intensities. The difference in Raman spectra may be due to the different distribution of cations in *M2*-*M5* sites (Alifirova et al. 2020).

The Raman spectrum of the **MD** shows broad and low-intensity bands. The strongest Raman bands are observed at 149, 297, 378, 422, 732, and 810 cm^{-1}. Other weaker bands can be detected at 177, 199, 508, and 567 cm^{-1}. Bands can be assigned according to Frost and Reddy (2011). Bands below 220 cm^{-1} can be tentatively assigned to molecular deformation and lattice modes. The 238–274 cm^{-1} and 300–560 cm^{-1} bands may correspond to U–O vibrations. The bands at 600–650 cm^{-1} are assigned to the Ti–O stretching vibrations. The bands at 732 and 811 cm^{-1} are due to the symmetric stretching vibrations of $(UO_2)^{2+}$.

Raman spectra of the **RD** sample represent many intensive bands: 117, 149, 177, 238, 297, 317, 350, 378, 422, 454, 642, 732 and 810 cm^{-1}. Raman bands splitting is observed in the range 100–500 cm^{-1}. The vibration mode at 567 cm^{-1} observed for the **MD** sample is not registered for the **RD**.

TG and DSC analysis

Figure 6 displays the TG and DSC curves. The mineral undergoes a color change and exhibits a porous texture after heating to 1300 °C. The TG curve reveals five stages of the mass loss.

The first endothermic effect with a peak at 121 °C corresponds to the loss of 0.42 wt.% due to the release of the adsorption water. A notable exothermic slope appeared in the DSC curve in the range of 529–747 °C. Notably, the mass has increased in the range 529–617 °C but returned to its decreasing trend after reaching 617 °C. The combination of the mass increase and exothermic effect suggests the possibility of the oxidation process for iron and other elements.

In the range 747–1215 °C, the TG curve exhibits a 0.38 wt.% mass loss. The DSC curve reveals an endothermic peak at 1248 °C. This effect is accompanied by a 0.26 wt.% mass loss in the TG curve. The shape of the endothermic peak suggests a partial melting of the sample. During the subsequent cooling, the DSC curve showed an exothermic peak

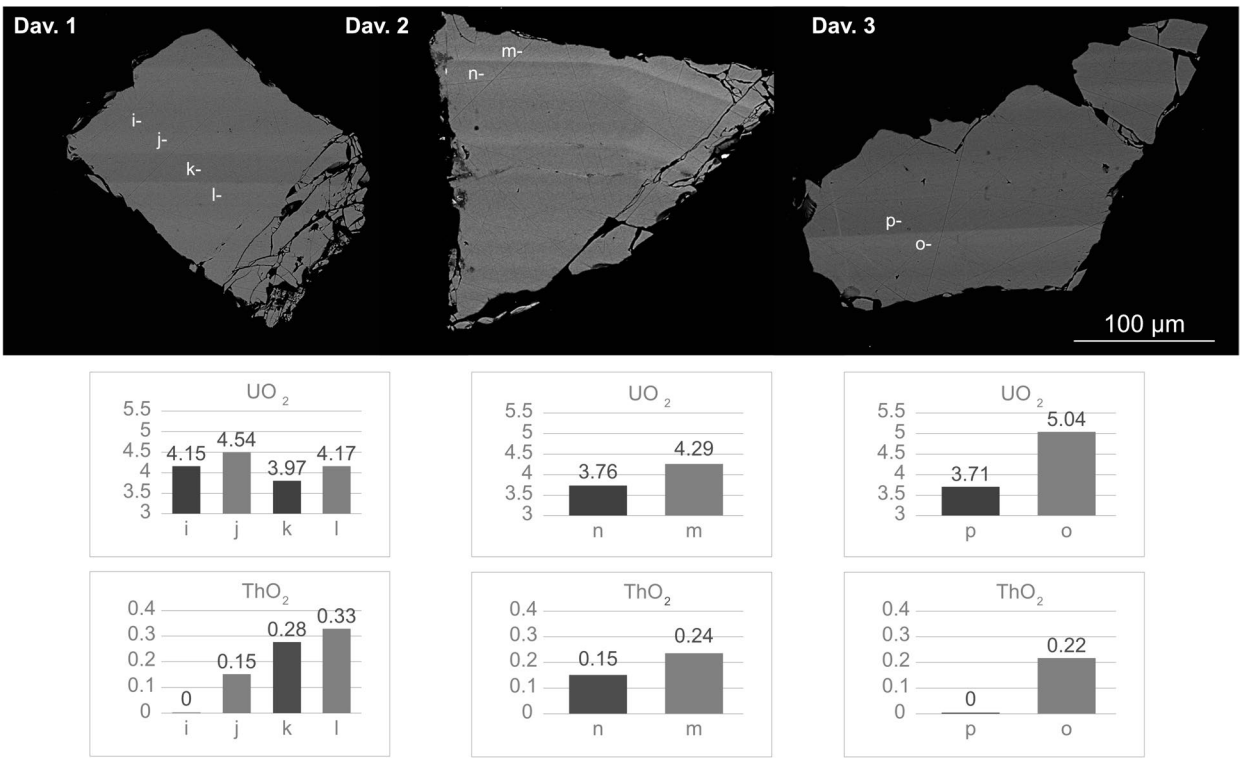

Fig. 3 BSE images of the metamict davidite-(La) (**MD**) grains. The BSE bright and dark areas differ due to the different uranium and thorium content (below)

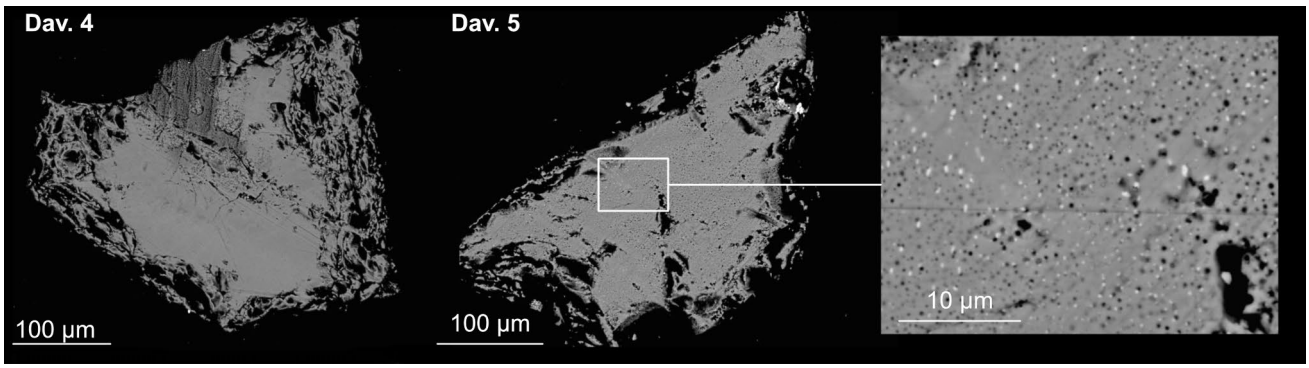

Fig. 4 BSE images of the recrystallized davidite-(La) (**RD**). The porous texture is shown to the right. Many bright dots with a size of less than 1 µm can be seen

at 1201 °C due to the crystallization of the partially melted material.

Figure 7 shows the X-ray powder pattern obtained for the sample after the thermal analysis. The following ICSD cards were employed: #100554 davidite-(La), #62679 rutile #291617 pseudobrookite, and #30670 ilmenite. The dominant phase in the sample is davidite-(La). Ilmenite (10.91 wt.%), rutile (2.22 wt.%) and pseudobrookite (2.66 wt.%) are the main decomposition products after the partial melting of the sample.

High-temperature X-ray diffraction of MD and the thermal expansion of RD

Figure 8a shows the evolution of the PXRD patterns of the **MD** in the range of 25–1200 °C. The peaks corresponding to davidite-(La) (ICSD #100554) gradually appear in the range 600–700 °C.

The **RD** unit-cell was refined at each temperature, employing the hexagonal lattice of the space group $R\,\overline{3}$, instead of the rhombohedral setting ($R\overline{3}$:R). The R_{wp} value

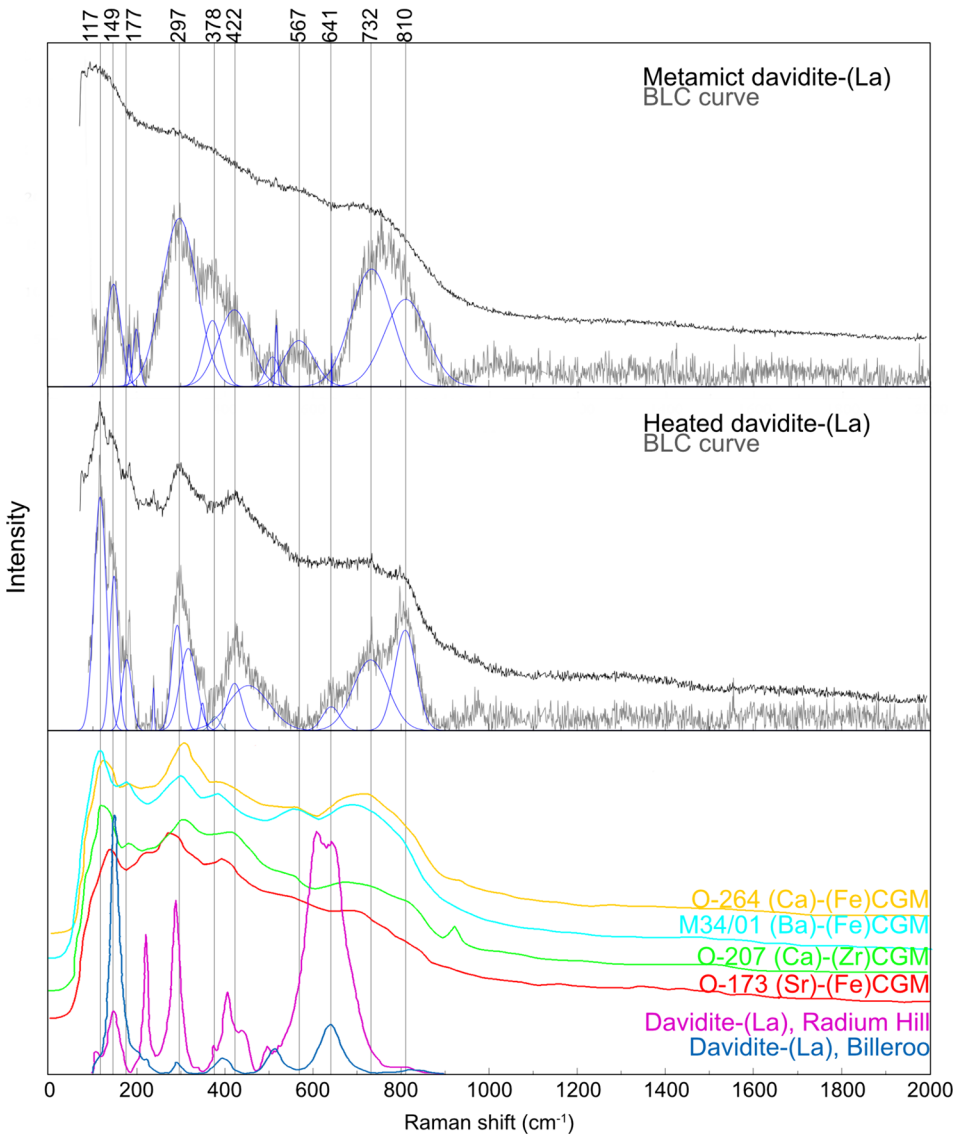

Fig. 5 Raman spectra of the **MD** and **RD**. Baseline correction (BLC) was performed using the program CrystalSleuth. Reference Raman spectra from Alifirova et al. (2020) and Frost and Reddy (2011) are given below

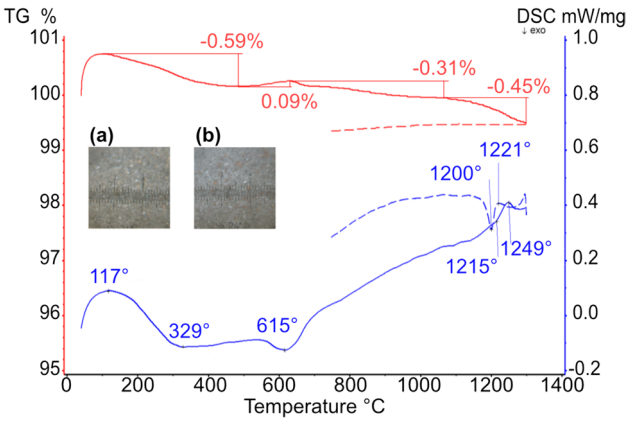

Fig. 6 TG and DSC curves for the **MD** and photographs of the sample before (**a**) and after (**b**) the heating/cooling cycle. Note the colour change of the probe after the experiment

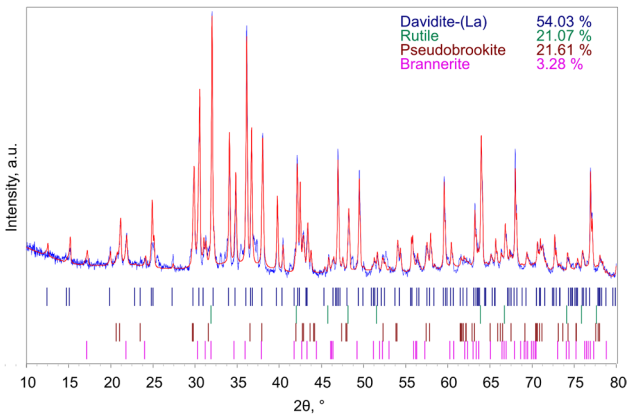

Fig. 7 Powder X-ray diffraction pattern (R_{wp} = 4.4%) for the Dav.1 sample after the thermal analysis

increases with the temperature rise from 9.88% to 12.74%, and the goodness-of-fit (GoF) increases from 1.63 to 1.94.

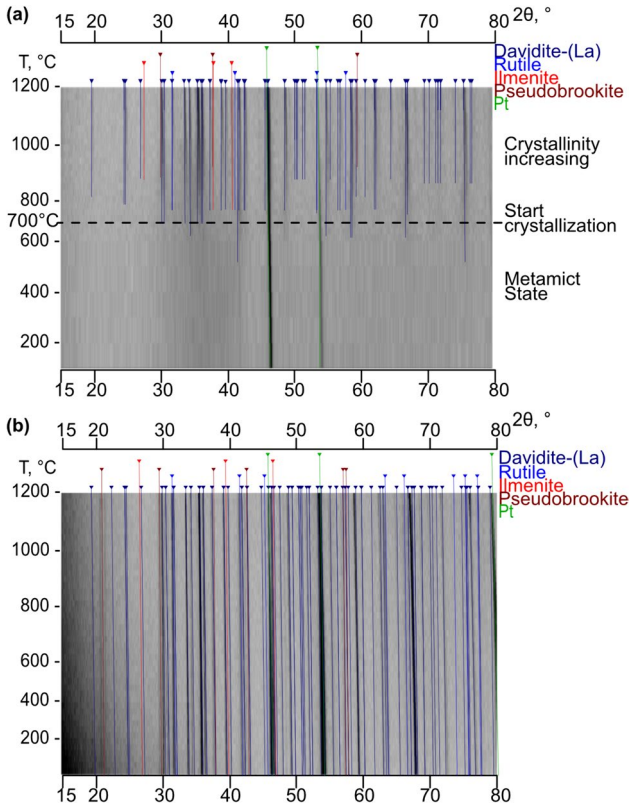

Fig. 8 Evolution of the powder diffraction patterns of the **MD** (**a**) and **RD** (b) as a function of temperature

The unit-cell parameters of the **RD** almost linearly increase upon heating (Fig. 9a). The unit-cell parameter *a* increases in the narrow range 10.364 (1)–10.491 (1) Å, while the *c* value increases from 20.858 (1) to 21.133 (1) Å. The unit-cell volume increases from 1940.39 (24) to 2014.62 (31) Å^3. The temperature dependence of the lattice parameters in the range of 25–1200 °C was approximated by the following polynomials of the second order:

$a\ (T) = 10.36332\ (43) + 0.0847\ (17)\cdot10^{-3}\cdot T + 0.0159\ (13)\cdot10^{-6}\cdot T^2$

$c\ (T) = 20.8546\ (13) + 0.1709\ (50)\cdot10^{-3}\cdot T + 0.0463\ (40)\cdot10^{-6}\cdot T^2$

$V\ (T) = 1939.69\ (24) + 47.47\ (94)\cdot10^{-3}\ T + 10.98\ (76)\cdot10^{-6}\cdot T^2$

Table 2 provides the thermal expansion coefficients (TEC) for **RD**. The average TEC along the *a* and *b* axes is $\overline{\alpha}_a = \overline{\alpha}_b = 9.96\ (3)\times10^{-6}\ °C^{-1}$, while the CTE along the *c* axis is somewhat more pronounced: $\overline{\alpha}_c = 10.79\ (4)\times10^{-6}\ °C^{-1}$. The observed character of the thermal expansion (Fig. 9b) is in agreement with the structure of davidite-(La) characterized by layers stacked along the *c* axis (Fig. 1). The volume coefficient α_V was calculated as follows: $\alpha_V = \alpha_{11} + \alpha_{22} + \alpha_{33} = \alpha_a + \alpha_b + \alpha_c$. It increases from 24.81 (47) $\times10^{-6}$ to 36.80 (48) $\times10^{-6}\ °C^{-1}$ in the temperature range 25–1200 °C.

Discussion

As confirmed by HTXRD and thermal analysis, the heat treatment induces recrystallization of the metamict davidite-(La) (**MD**). The temperature range of this phenomenon

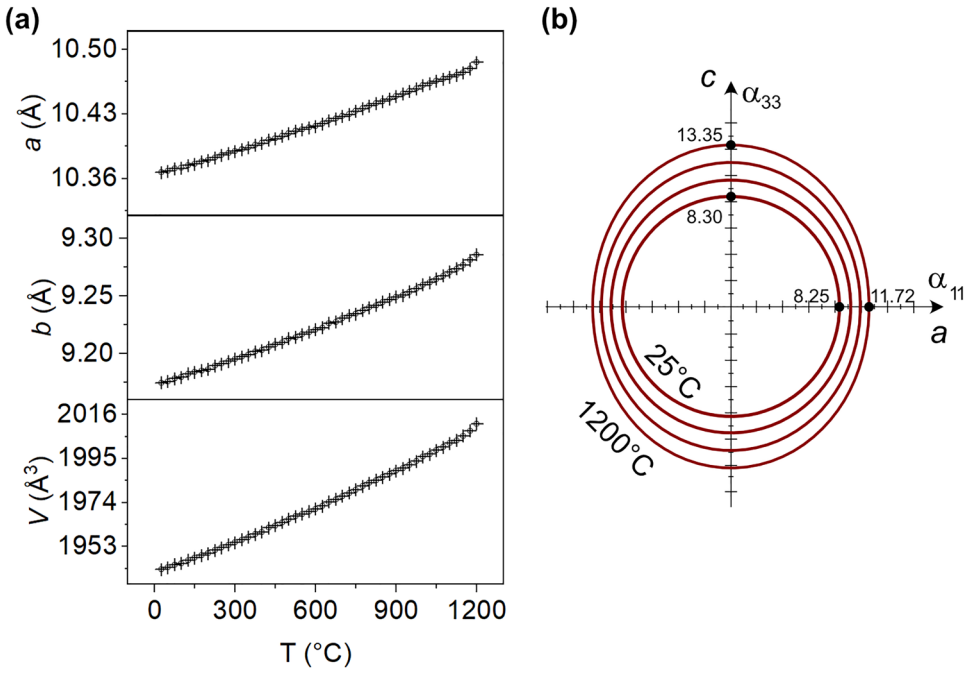

Fig. 9 Temperature dependence of the unit-cell parameters for **RD** (**a**). The main sections of the thermal expansion tensor (**b**). Values of the TEC are multiplied by 10^{-6} ($°C^{-1}$)

Table 2 TEC for davidite-(La) (**RD**) at different temperatures

T, °C	TEC, $\times 10^{-6}$ °C^{-1}			
	$\alpha_{11}=\alpha_a$	$\alpha_{22}=\alpha_b$	$\alpha_{33}=\alpha_c$	α_V
25	8.25(15)	8.25(15)	8.30(23)	24.81(47)
100	8.48(14)	8.48(14)	8.63(20)	25.59(41)
200	8.78(11)	8.78(11)	9.07(17)	26.62(34)
300	9.07(8)	9.07(8)	9.50(13)	27.65(26)
400	9.37(6)	9.37(6)	9.93(9)	28.68(20)
500	9.67(4)	9.67(4)	10.36(7)	29.71(14)
600	9.96(3)	9.96(3)	10.79(5)	30.73(12)
700	10.26(4)	10.26(4)	11.22(7)	31.75(14)
800	10.55(6)	10.55(6)	11.65(9)	32.77(20)
900	10.85(8)	10.85(8)	12.08(13)	33.78(26)
1000	11.14(11)	11.14(11)	12.51(16)	34.79(33)
1100	11.43(13)	11.43(13)	12.93(20)	35.80(40)
1200	11.72(16)	11.72(16)	13.35(24)	36.80(48)

as determined by the HTXRD is between 600 and 700 °C, whereas the DSC curve exhibits a peak at 615 °C. The **MD** has a massive texture, in contrast to the **RD** ones having a porous texture. HTXRD results indicate that the unit-cell volume of the **RD** increases by 73.23 Å^3 within the temperature range of 25–1200 ºC.

Furthermore, the DSC curve exhibits an endothermic effect at 1215 °C, suggesting a partial melting of the **RD** and the formation of minor phases. Following the heating process, the **RD** exhibits an inhomogeneous distribution of elements. It has been found that certain elements are partially or completely excluded from the **MD** structure after heating, thus forming relatively stable phases: ilmenite, rutile and pseudobrookite. Previously, it was reported that pseudobrookite is a common by-product phase that arises as a result of the hydrothermal synthesis of "uranium davidite $(U,Fe,Ti)_{21}O_{39}$" (Korolev et al. 1977).

Multiphase ceramics were designed for the immobilization and disposal of high-level radioactive wastes (HLW) (Ringwood 1985). To understand the thermophysical properties of ceramics, it is necessary to study their constituent components (Yudintsev et al. 2022). The material's expansion at elevated temperatures and radiation is the crucial feature for HLW ceramics. Previously, numerous studies were conducted to examine the thermal characteristics of the phases proposed for such applications. The monoclinic zirconolite $CaZrTi_2O_7$ has the following TECs in the temperature range 25–1200 °C: $\overline{\alpha}_a = 11.35\ (25) \times 10^{-6}$, $\overline{\alpha}_b = 8.72\ (22) \times 10^{-6}$, $\overline{\alpha}_c = 10.0\ (5) \times 10^{-6}$ ºC^{-1} (Ball et al. 1992). TECs observed for the orthorhombic perovskite $CaTiO_3$ are: $\overline{\alpha}_a = 7.86\ (30) \times 10^{-6}$, $\overline{\alpha}_b = 13.46\ (17) \times 10^{-6}$; $\overline{\alpha}_c = 16.55\ (26) \times 10^{-6}$ ºC^{-1} (Ball et al. 1992). The thermal expansion of the uranium titanate, a mineral brannerite UTi_2O_6, was recently investigated. Its monoclinic structure exhibits significant anisotropy: $\overline{\alpha}_a = 9.46\ (50) \times 10^{-6}$ ºC^{-1}, $\overline{\alpha}_b = 5.30\ (34) \times 10^{-6}$ ºC^{-1}; $\overline{\alpha}_c = 7.54\ (42) \times 10^{-6}$ ºC^{-1} (Chen et al. 2023). In the present work, the TECs of davidite-(La) (**RD**) for the temperature range 25–1200 °C were obtained: $\overline{\alpha}_a = \overline{\alpha}_b = 9.96\ (3) \times 10^{-6}$; $\overline{\alpha}_c = 10.79\ (4) \times 10^{-6}$ ºC^{-1}. Hence, the thermal expansion of davidite- (La) is almost isotropic, exhibiting the most superior thermal performance in comparison to the other mineral phases cited above.

Kutty et al. (1994) conducted a study on several REE pyrochlores $Ln_2M_2O_7$ (Ln = La—Gd; M = Zr, Hf). In the temperature range of 25–1227 ºC, $La_2Zr_2O_7$ exhibits a volume TEC ranging from 23.1 to 27.8×10^{-6} ºC^{-1}, whereas $Gd_2Hf_2O_7$ shows an $\alpha_V = 29.1 - 34.3 \times 10^{-6}$ ºC^{-1}. The volume coefficient of thermal expansion for davidite-(La) ranges from 24.81 (47) to 36.80 $(48) \times 10^{-6}$ ºC^{-1}, which is comparable to that of $Ln_2M_2O_7$ pyrochlores previously studied.

Conclusion

To the best of our knowledge, our study presents the first report on the thermal expansion of the crystalline davidite-(La) (**RD**) with a high content of various radionuclides. Our findings indicate that davidite-(La) exhibits a low TEC, indicating its thermophysical stability in contrast to many other phases utilized for nuclear waste immobilization. Furthermore, it exhibits an almost isotropic thermal expansion. All thermal expansion coefficients exhibit a linear increase with the increase in temperature. The α_c is somewhat more sensitive to the temperature rise. The davidite-(La) structure is both flexible and stable, enabling it to accommodate different radionuclides. Despite the limitation of the experiment temperature to 25–1200 °C, the trends of the unit-cell parameters, expressed as derived polynomials, can be utilized to simulate the TEC at higher temperatures.

Acknowledgements Technical support by the X-ray diffraction and Geomodel (project 103752493) SPbSU Resource Centers is gratefully acknowledged. R. Chen thanks the Region Hauts de France for financial support and the Chevreul Institute (FR 2638), Region Hauts-de-France, and FEDER for funding the X-ray diffractometers.

Author contributions All authors have equally contributed to the work described. R. Chen and O.I. Siidra: Research design and methodology; R. Chen: writing-original draft preparation; O.I. Siidra and R. Chen: writing-review and editing; R. Chen, V.A. Firsova, O.I. Siidra: thermal expansion analysis; R. Chen and V.L. Ugolkov: thermal analysis. N.S. Vlasenko and R. Chen: electron microprobe analysis. V.N. Bocharov and R. Chen: Raman spectroscopy. O.I. Siidra, A. M. Arevalo-Lopeze and M. Colmont: supervision.

Funding Not applicable.

Availability of data and materials Not applicable.

Declarations

Competing interests The authors declare that they have no known competing financial interests or personal relationships that could have appeared to influence the work reported in this paper.

Ethical approval Not applicable.

References

Alifirova T, Rezvukhin D, Nikolenko E, Nikolenko E, Pokhilenko L, Zelenovskiy P, Sharygin I, Korsakov A, Shur V (2020) Micro-Raman study of crichtonite group minerals enclosed into mantle garnet. J Raman Spectrosc 51:1493–1512

Ball CJ, Thorogood GJ, Vance ER (1992) Thermal expansion coefficients of zirconolite ($CaZrTi_2O_7$) and perovskite ($CaTiO_3$) from X-ray powder diffraction analysis. J Nucl Mater 190:298–301

Bruker AXS (2011). TOPAS, V5.0. (Computer Software), Bruker AXS, Karlsruhe, Germany.

Bubnova RS, Firsova VA, Volkov SN, Filatov SK (2018) Rietveld-ToTensor: Program for processing powder X-ray diffraction data under variable conditions. Glass Phys Chem 44:33–40

Chen R, Siidra OI, Firsova VA, Arevalo-Lopez A, Colmont M, Ugolkov VL, Bocharov VN (2023) The chemistry, recrystallization and thermal expansion of brannerite from Akchatau, Kazakhstan. Materials 16:1719

Frost RL, Reddy BJ (2011) The effect of metamictization on the Raman spectroscopy of the uranyl titanate mineral davidite (La,Ce)$(Y,U,Fe^{2+})(Ti,Fe^{3+})_{20}(O,OH)_{38}$. Radiat Eff Defect S 166:133–136

Gatehouse BM, Grey IE, Kelly PR (1979) The crystal structure of davidite. Am Mineral 64:1010–1017

Gong WL, Ewing RC, Wang LM, Xie HS (1994) Crichtonite structure type ($AM_{21}O_{38}$ and $A_2M_{19}O_{36}$) as a host phase in crystalline waste form ceramics. Mater Res Soc Symp - Proc 353:807–815

Korolev KG, Gaidukova VS, Rumyantseva GV (1977) Structural and morphological features and composition of davidite [in Russian]. Textures and structures of uranium ores of endogenous deposits. Moscow Atomizdat, Moscow, pp 51–57

Kutty KVG, Rajagopalan S, Mathews CK, Varadaraju UV (1994) Thermal expansion behaviour of some rare earth oxide pyrochlores. Mater Res Bull 29:759–766

Lottermoser BG, Ashley PM (2005) Environmental review of the Radium Hill mine site, South Australia. World Min Surf Undergr 57:2–6

Ludwig KR, Cooper JA (1984) Geochronology of Precambrian granites and associated U-Ti-Th mineralization, northern Olary province, South Australia. Contrib Mineral Petr 86:298–308

Lumpkin GR (2006) Ceramic waste forms for actinides. Elements 2:365–372

Rastsvetaeva RK (2020) Crichtonite and its family: the story of the discovery of two new minerals. Priroda 8:39–47 (In Russian)

Rigaku, (2016) PDXL: Integrated X-ray powder diffraction software. Rigaku Corporation, Oxford, U.K.

Ringwood AE (1985) Disposal of high-level nuclear wastes: a geological perspective. Mineral Mag 49:159–176

Whittle AWG (1954) The radioactive minerals of south Australia and their petrogenetic significance. J Geol Soc Australia 2(1):21–45

Whittle AWG (1959) The nature of davidite. Econ Geol 54(1):64–81

Yudintsev SV, Stefanovskii SV, Kir'yanova OI, Lian J, Ewing R, (2001) Radiation resistance of fused titanium ceramic for actinide immobilization. At Energy 90:487–494

Yudintsev SV, Nickolsky MS, Ojovan MI, Stefanovsky OI, Nikonov BS, Ulanova AS (2022) Zirconolite polytypes and murataite polysomes in matrices for the REE—actinide fraction of HLW. Materials 15:6091

Zhang Y, Karatchevtseva I, Qin M, Middleburgh SC, Lumpkin GR (2013) Raman spectroscopic study of natural and synthetic brannerite. J Nucl Mater 437:149–153